Eddy heat and salt transports in the South China Sea and their seasonal modulations

Gengxin Chen,[1] Jianping Gan,[2] Qiang Xie,[1,3] Xiaoqing Chu,[1] Dongxiao Wang,[1] and Yijun Hou[4]

Received 10 November 2011; revised 27 March 2012; accepted 30 March 2012; published 12 May 2012.

[1] This study describes characteristics of eddy (turbulent) heat and salt transports, in the basin-scale circulation as well as in the embedded mesoscale eddy found in the South China Sea (SCS). We first showed the features of turbulent heat and salt transports in mesoscale eddies using sea level anomaly (SLA) data, in situ hydrographic data, and 375 Argo profiles. We found that the transports were horizontally variable due to asymmetric distributions of temperature and salinity anomalies and that they were vertically correlated with the thermocline and halocline depths in the eddies. An existing barrier layer caused the halocline and eddy salt transport to be relatively shallow. We then analyzed the transports in the basin-scale circulation using an eddy diffusivity method and the sea surface height data, the Argo profiles, and the climatological hydrographic data. We found that relatively large poleward eddy heat transports occurred to the east of Vietnam (EOV) in summer and to the west of the Luzon Islands (WOL) in winter, while a large equatorward heat transport was located to the west of the Luzon Strait (WLS) in winter. The eddy salt transports were mostly similar to the heat transports but in the equatorward direction due to the fact that the mean salinity in the upper layer in the SCS tended to decrease toward the equator. Using a 2½-layer reduced-gravity model, we conducted a baroclinic instability study and showed that the baroclinic instability was critical to the seasonal variation of eddy kinetic energy (EKE) and thus the eddy transports. EOV, WLS, and WOL were regions with strong baroclinic instability, and, thus, with intensified eddy transports in the SCS. The combined effects of vertical velocity shear, latitude, and stratification determined the intensity of the baroclinic instability, which intensified the eddy transports EOV during summer and WLS and WOL during winter.

Citation: Chen, G., J. Gan, Q. Xie, X. Chu, D. Wang, Y. Hou (2012), Eddy heat and salt transports in the South China Sea and their seasonal modulations, *J. Geophys. Res.*, *117*, C05021, doi:10.1029/2011JC007724.

1. Introduction

[2] The South China Sea (SCS) is the largest marginal sea in the tropics and has a maximum depth of over 5,000 m. The southwest monsoon prevails over the whole region in summer, whereas a stronger northeast monsoon dominates the SCS in winter. The upper-layer ocean circulation of the SCS is driven mainly by the monsoons [*Hu et al.*, 2000; *Qu*, 2000]. In general, the seasonal circulation pattern can be separated into a northern and a southern circulation. During winter, a strong cyclonic gyre forms and merges with a southern cyclonic gyre to form a basin-wide cyclonic circulation pattern [*Dippner et al.*, 2007]. In summer, wind stress curls produce a cyclonic northern gyre and an anticyclonic southern gyre that form a dipole with a jet streaming away from the Vietnamese coast [*Fang et al.*, 2002; *Gan et al.*, 2006; *Gan and Qu*, 2008]. The geographic distribution of eddy energy shows that the higher EKE is to the east of Vietnam and to the west of Taiwan [*Chen et al.*, 2009]. These areas also have high mesoscale eddy activity [*Wang et al.*, 2008; *Chen et al.*, 2011a].

[3] The ocean plays an important role in closing the global heat balance. The mean ocean circulation carries about one third to one half of the excess heat from the tropics to the poles. The ocean is a turbulent medium in which the mean circulation is generally much weaker than its time-varying signals [*Qiu and Chen*, 2005]. Many studies have focused on meridional eddy transports (or turbulent transports) in the ocean. *Stammer* [1998] concluded that high poleward eddy heat transports are associated with western boundary currents such as the Gulf Stream and the Kuroshio as well as the

[1]State Key Laboratory of Tropical Oceanography, South China Sea Institute of Oceanology, Chinese Academy of Sciences, Guangzhou, China.
[2]Division of Environment and Department of Mathematics, Hong Kong University of Science and Technology, Hong Kong, China.
[3]Sanya Institute of Deep-Sea Science of Engineering, Chinese Academy of Sciences, Sanya, China.
[4]Key Laboratory of Ocean Circulation and Waves, Institute of Oceanology, Chinese Academy of Sciences, Qingdao, China.

Corresponding author: D. Wang, State Key Laboratory of Tropical Oceanography, South China Sea Institute of Oceanology, Chinese Academic of Science, 164 West Xingang Rd., Guangzhou 510301, China. (dxwang@scsio.ac.cn)

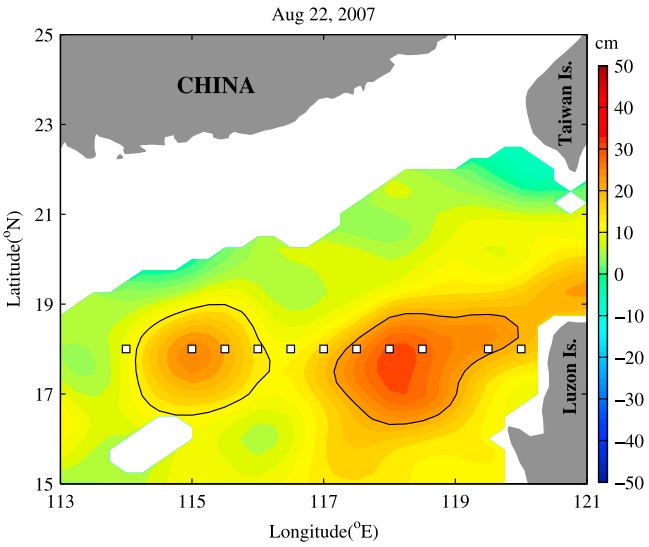

Figure 1. SLA distribution (color) on 22 August 2007. White squares denote the CTD locations. Black contour marks the edge of an eddy. The altimetry data over the shelf shallower than 500 m is discarded.

North Equatorial Counter Current and the Antarctic Circumpolar Current. His estimate of eddy transport for the global ocean was in the form of $v'\lambda' = -\kappa\nabla_h\bar{\lambda}$, where $\bar{\lambda}$ is a time-mean tracer field. Here he adopted a "mixing length" hypothesis and proposed an alternative formula for estimating eddy diffusivity. In the subtropical North Pacific, *Qiu and Chen* [2005] pointed out that most of the eddy-induced heat transport was in the top 200 m. Large meridional heat transports are found in the Kuroshio Extension region and in the subtropical North Pacific along a southwest–northeast-tilting band between Taiwan and the Midway Islands. Eddy fluxes are important contributors in total heat flux in western boundary currents of all oceans and could affect heat balances of other ocean regions [*Wunsch*, 1999] and mesoscale eddies are a major contributor to observed time-varying ocean heat transport [*Roemmich et al.*, 2001].

[4] An oceanic mesoscale eddy, or eddy vortex, is an enclosed-circular motion with a typical diameter of 50–150 km. Mesoscale eddies play an essential role in the transport of heat, salt, and chemical substances. Previous studies have revealed that mesoscale eddies appear frequently in the SCS and significantly affect the structure of temperature and salinity. *Chen et al.* [2010a] suggested that the Luzon Warm Eddy (LWE) incorporates higher temperature and salinity water from the Kuroshio and carries it westward. *Chen et al.* [2010b] examined the impact of a pair of eddies on the thermocline off eastern Vietnam. They pointed out that when the two eddies were strong, the difference in the thermocline depths of the cyclonic eddy and of the anticyclonic eddy was more than 60 m. *Chen et al.* [2011a] concluded that a cyclonic eddy could lead to a shallower and thinner thermocline and significantly strengthen the thermocline intensity, whereas an anticyclonic eddy could deepen the thermocline, thickening and weakening the thermocline intensity to a certain degree. The halocline impacted by cyclonic eddies is also shallower and thinner than that impacted by anticyclonic eddies. *Hu et al.* [2011] showed that the upward dome of isotherms and isohalines in the central part of a cyclonic eddy was formed by the combination of the upward velocity around the center of the eddy and the downward velocity to the southwest and to the east of the center. The effects of mesoscale eddies on heat, salt and water masses in regions other than the SCS have also been frequently reported. For example, *Itoh and Yasuda* [2010] showed that warm anticyclonic eddies and cold anticyclonic eddies exist in the western boundary region of the North Pacific. *Kamenkovich et al.* [2011] verified the significant effects of the mesoscale eddy on the accuracy of reconstructing temperature, salinity, and velocities of the North Atlantic from Argo measurements and trajectories.

[5] However, so far, research on eddy transports in the SCS is limited. In our study, we examined eddy transports in basin-scale general circulation as well as in the embedded mesoscale eddies. We first investigated the characteristics of eddy transport in the mesoscale eddy by examining eddies detected by altimeter, in situ data, and Argo profiles (section 3). We estimated meridional eddy heat and salt transports based on v', T' and S' values that were deviations from their respective means. In section 4, we estimated eddy transports in the SCS basin using an eddy diffusivity method and using altimeter data and climatological WOA01 data with a 1/4° × 1/4° resolution [*Boyer et al.*, 2005]. In section 5, we present a 2½-layer reduced-gravity model that we adopted to explore the underlying physics of the observed seasonal modulations of eddy transports. section 6 summarizes our results.

2. Data and Methods

2.1. Altimetry, In Situ, and Argo Data

[6] We used the sea level anomaly (SLA) data (October 1992 to October 2009) from a merged product of TOPEX/POSEIDON, Jason-1, Envisat, and European Research Satellite (ERS) altimeter observations to identify and track eddies in the SCS. The product is available in a 7-day cycle with 1/4° × 1/4° resolution.

[7] The in situ temperature and salinity data were conductivity-temperature-depth (CTD) measurements from 11 stations (white squares in Figure 1) along 18°N between 114°E and 120°E sampled from 20 to 24 August 2007. The station depths were all greater than 1,500 m and the vertical resolution of the data was 1 m. We used the in situ temperature and salinity data to examine mesoscale eddy-induced transport features.

[8] The global Argo project was initiated in 1998 to collect temperature and salinity profiles of the world's oceans on a broad spatial scale. The data recorded by 63 Argo floats in the SCS before October 2009 (Figure 2) were used to further determine the eddy transport features.

2.2. Basin-Scale Eddy Transport

[9] The basin-scale, eddy heat and salt transports were estimated using eddy diffusion $-\rho C_p\kappa\partial\bar{T}/\partial y$ and $-\rho/S_0\kappa\partial\bar{S}/\partial y$, respectively [*Stammer*, 1998], where the diffusion coefficient κ was obtained according to $\kappa = 2\alpha K_E T_{alt}$. K_E is an estimate of near-surface EKE from altimeter data, T_{alt} is the integral time scale obtained from the autocovariance of the altimetric sea surface height data [*Stammer*, 1997], and α (~0.005) is a correlation coefficient that determines the efficiency of

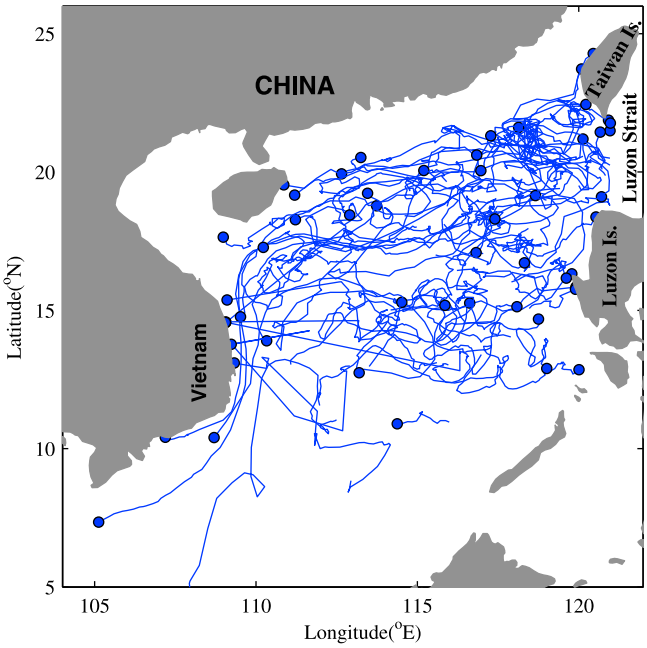

Figure 2. Trajectories of the 63 Argo floats in the SCS before October 2009.

individual eddies to mix tracer particles. $\bar{T}$ and $\bar{S}$ are defined as the mean temperature and salinity averaged in the upper water column, respectively. Cp = 4187 J/Kg/°C and S_0 = 34.48.

2.3. A 2½-Layer Reduced-Gravity Model

[10] We used a 2½-layer reduced-gravity model [*Qiu*, 1999] to investigate the seasonal modulations of eddy transports. Under the quasi-geostrophic approximation, the linearized equations governing the perturbation potential vorticity q_n (n = 1 and n = 2 refer to the surface and lower layers, respectively) are

$$\left(\frac{\partial}{\partial t}+U_n\frac{\partial}{\partial x}\right)q_n+\frac{\partial \Pi_n}{\partial y}\frac{\partial \phi_n}{\partial x}=0, \tag{1}$$

where ϕ_n is the perturbation stream function; U_n is the zonal mean velocity; and Π_n is the mean potential vorticity in each layer. If U_n is meridionally uniform, then q_n and the meridional gradient of Π_n can be expressed by

$$q_n=\nabla^2\phi_n+\frac{(-1)^n}{\gamma_2\delta_n\lambda^2}(\phi_1-\phi_2-\gamma_n\phi_2), \tag{2}$$

$$\Pi_{ny}=\beta-\frac{(-1)^n}{\gamma_2\delta_n\lambda^2}(U_1-U_2-\gamma_nU_2), \tag{3}$$

where

$$\delta_n=\frac{H_n}{H_2},\gamma_n=\frac{\rho_n-\rho_1}{\rho_3-\rho_2}\quad\text{and}\quad\lambda=\frac{1}{f_0}\sqrt{\frac{\rho_3-\rho_2}{\rho_0}gH_2}. \tag{4}$$

[11] In the above equations H_n is the mean thickness of layer n; ρ_n is the density of layer n; β is the meridional gradient of the Coriolis parameter; f_0 is the Coriolis parameter at the reference latitude; ρ_0 is the reference density; and ρ_3 is the density of the motionless layer at depth. According to equation (4), δ gives the layer depth ratio and γ is the stratification ratio.

[12] The stability of the system can be analyzed by seeking the normal mode solution: ϕ_n = Re[A_n exp $i(kx+ly-kct)$]. Substituting ϕ_n into equation (2) and requiring nontrivial solutions for A_n leads to a quadratic equation for the complex phase speed $c=c_r+ic_i$

$$c^2-\left(U_1+U_2-\frac{P+Q}{R}\right)c+\left(U_1U_2+\frac{\Pi_{1y}\Pi_{2y}}{R}-\frac{U_1P}{R}-\frac{U_2P}{R}\right)=0, \tag{5}$$

where

$$P=\left(K^2+1/\gamma_2\delta_1\lambda^2\right)\Pi_{2y},\ Q=\left[K^2+(1+\gamma_2)/\gamma_2\lambda^2\right]\Pi_{1y},\quad\text{and}$$
$$R=PQ/\Pi_{1y}\Pi_{2y}-1/{\gamma_2}^2\delta_1\lambda^4. \tag{6}$$

[13] We used this analysis of the stability derived from the model to examine the baroclinic stability of circulation and its associated eddy heat and salt transports in the SCS in section 5.

3. Eddy Transport Features in the Mesoscale Eddy

[14] We examined the eddy transport features in the mesoscale eddy by combining in situ hydrographic sections that cut through two anticyclonic eddies in the northern SCS with 375 profiles affected by eddies obtained from Argo floats [*Chen et al.*, 2010a].

3.1. Individual Eddy Features

[15] The SLA distribution on 22 August 2007 (colored shading in Figure 1) shows two anticyclonic eddies in the northern SCS. The outer most enclosed SLA contours identified by the winding angle method correspond to the edges of the two eddies [*Chaigneau et al.*, 2008] (black contours in Figure 1). By tracking the motion of the two eddies, we found that the eastern one is the LWE, which is a seasonal eddy generated northwest of the Luzon Islands. The detailed evolution of the two eddies is described in *Nan et al.* [2011].

[16] We removed climatological *T-S* profiles from the observed ones to depict the anomalous vertical *T-S* structures of the two eddies shown in Figures 3b, 3c, 4b and 4c (one next to the Luzon Islands and one further to the west). Here, the climatological *T-S* profiles were obtained by interpolating the monthly WOA01 temperature and salinity to the CTD profile positions and times of the year. This was similar to what *Qiu and Chen* [2005] did in their work. Figures 3b, 3c, 4b and 4c show that the obvious warm anomalies were located at 40–300 m, with a maximum of 2–3°C, which were accompanied by low salinity anomalies at 20–200 m. The maximum salinity anomaly was 0.2, located around 80 m.

[17] With the anomalous temperature and salinity profiles, we calculated the geostrophic velocity (Figures 3a and 4a) of the eddies using the thermal wind relation and choosing 1,500 m as the reference level. The geostrophic velocity was

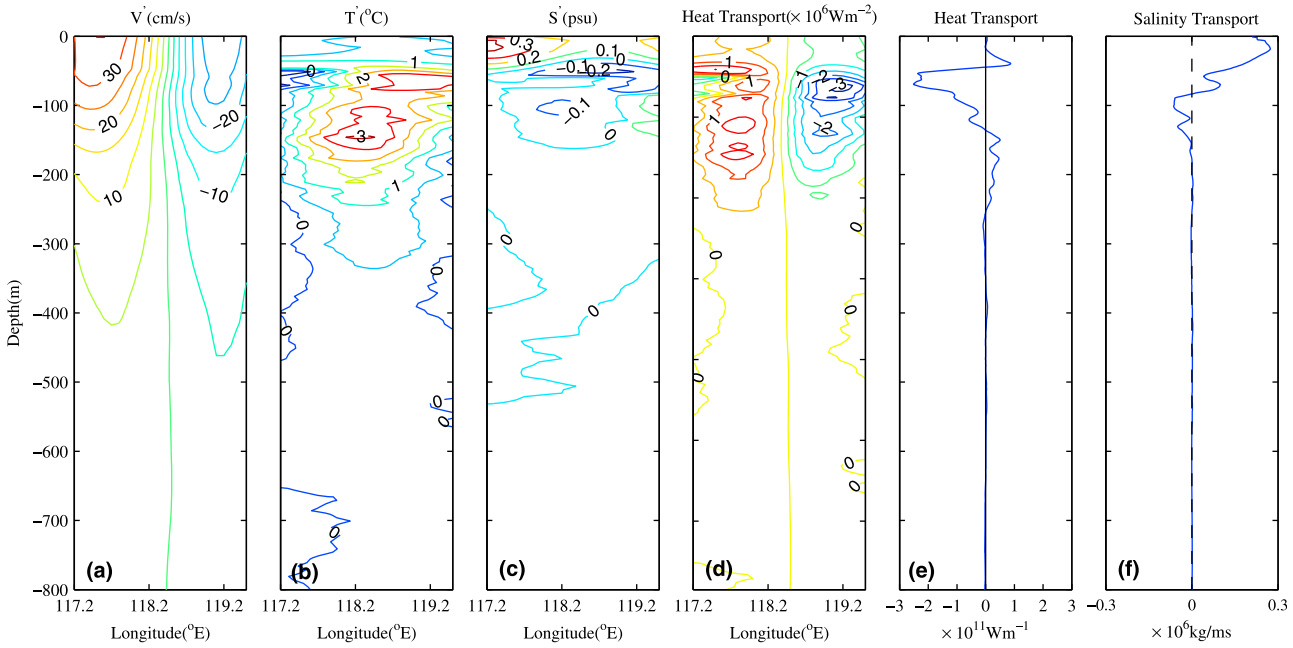

Figure 3. (a) Meridional geostrophic flow (cm/s); (b) temperature anomaly (°C); (c) salinity anomaly (psu); (d) heat transport ($\rho C_P v'T'$) distribution associated with the anticyclonic eddy next the Luzon Island detected on 22 August 2007; (e) heat transport integrated across the eddy; and (f) salt transport integrated across the eddy.

stronger in the upper 400 m, with a maximum speed larger than 0.30 m/s near the surface layer. The distributions of heat transport $\rho C_P v'T'$ inside the two eddies are shown in Figures 3d and 4d. The heat transport in the two anticyclonic eddies is positive (northward) in the western part and negative (southward) in the eastern part, with a relatively stronger value of O(10^6) W/m^2 at 40–300 m. We integrated across each eddy to see that the heat transports were strongly depth-dependent (Figures 3e and 4e). With relatively small T' in the upper layer, the heat transport was weak. The stronger transport within the thermocline was caused by larger T' and its spatially asymmetric distribution in the eddy center (Figures 3b and 4b). The total eddy heat transports induced by the two anticyclonic eddies were −6.910 TW (1 TW = 10^{12}W) and −10.103 TW. Differing from the heat transports, the stronger salt transports $\rho/S_0 v'S'$ were in the mixed layer (Figures 3f and 4f). The total meridional eddy salt transport was 1.139×10^7 and -5.894×10^6 kg/s for the eddy next to

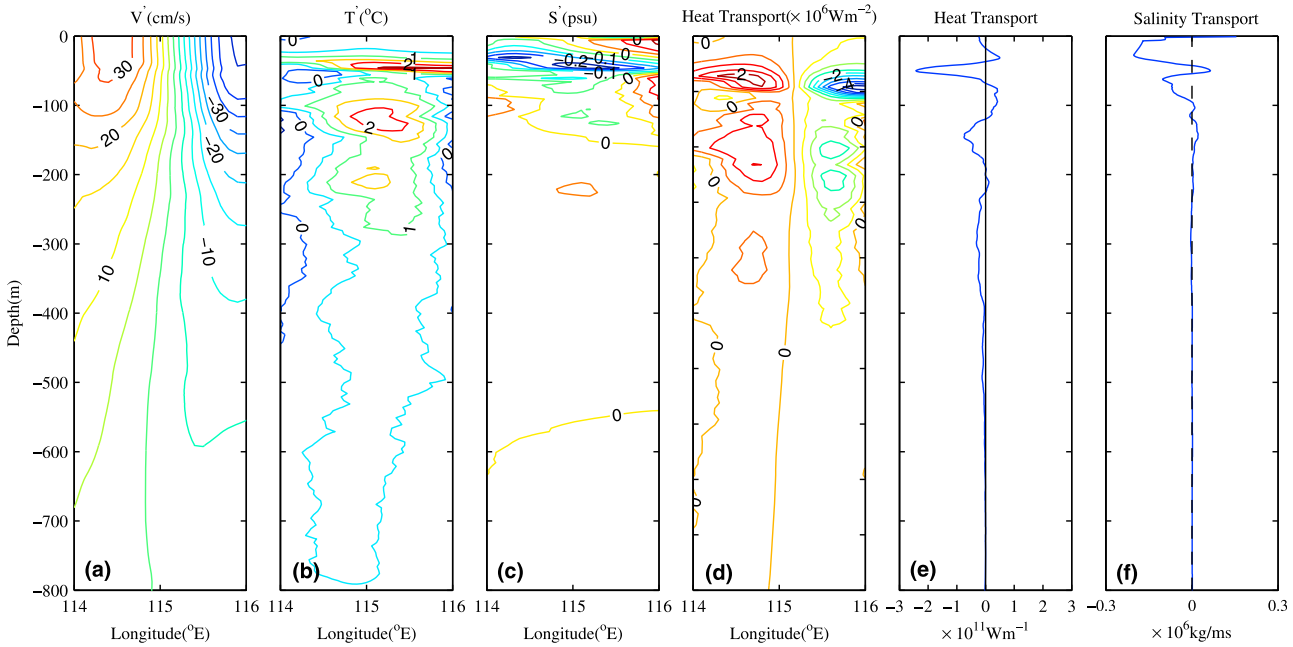

Figure 4. Same as Figure 3, except for another anticyclonic eddy detected on 22 August 2007.

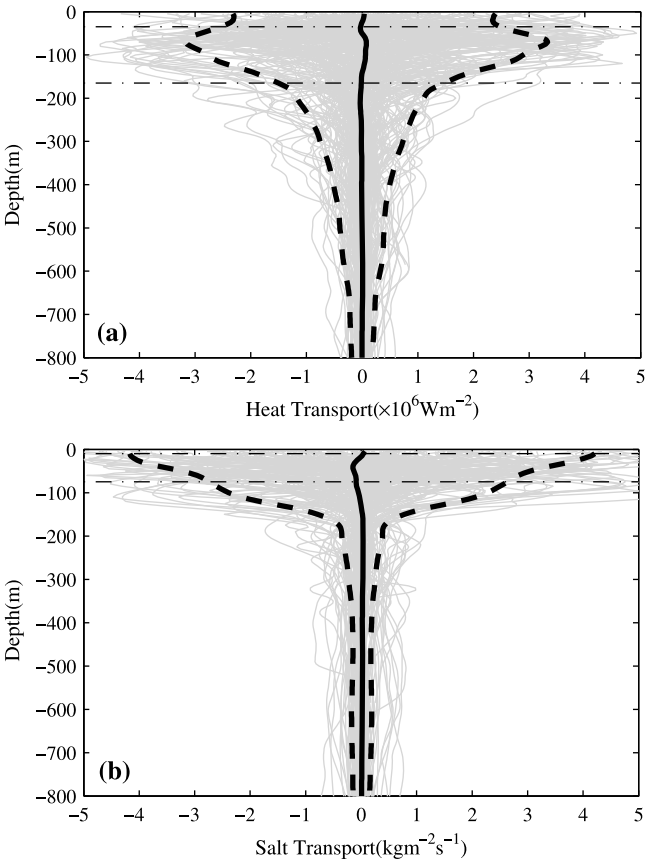

Figure 5. Eddy-induced turbulent (a) heat and (b) salt transports examined by the 375 Argo profiles affected by mesoscale eddies in the SCS before October 2009. Gray lines show the turbulent transport corresponding to each profile. The black solid line and the black dashed lines represent the mean value and the upper and lower 2σ of the average, respectively. Dash-dotted lines indicate the ranges of the thermocline and halocline.

Luzon Island and the eddy further to the west, respectively. Most of the salt transport was in the top 100-m. The contrasting positive and negative salt transports in these two eddies arose from the opposite v' at the two sides of eddies as well as the tilt of S'. For example, S' in the eddy next to Luzon Island and the eddy farther to the west tilted eastward and westward with depth, respectively. This leads to differing S' east and west of the eddy centers (Figures 3c and 4c), and thus a poleward and an equatorward transport, respectively (Figures 3f and 4f). Further investigations into eddy transport features in the mesoscale eddy are reported in section 3.2.

3.2. Statistical Features

[18] The data recorded by the 63 Argo floats (Figure 2) are used to further determine the eddy transport features. We use the available Argo profiling data in the following way:

[19] 1. First, for each consecutive pair of Argo *T-S* profiles (separated nominally by 10 days), we removed the climatological *T-S* profiles based on the WOA01 data following *Qiu and Chen* [2005]. From the paired anomalous *T-S* profiles, we calculated the meridional geostrophic velocity v' by letting the reference level be the smaller effective observation depth of the paired profiles. Data with a maximum observation depth less than 500 m were discarded. The average distance between Argo profiles that are 10 days apart is 19 km. Profiles with distance less than 50 km account for 94% of all the 3506 paired profiles. Profiles with distance greater than 100 km are infrequent, only 28 in number. Therefore, the estimated geostrophic velocity can be reasonably accurate.

[20] 2. Then, we followed *Chen et al.* [2011a] and used the winding angle method on 17 years of altimeter data and detected 827 eddies in the SCS. By combining the positions and time information of these eddies and Argo profiles, we obtained a total of 375 valid Argo profiles that were affected by eddies. All the corresponding distances of these profiles are less than 100 km with a most likely distance ~17 km.

[21] 3. Finally, using these affected Argo profiles, we obtained the eddy-induced turbulent heat and salt transports.

[22] The eddy-induced turbulent transports of the 375 Argo profiles are shown in Figure 5. A 2σ filter was applied to the transports at each depth to eliminate large uncertainties associated with the way they were computed. The parameter σ is the standard deviation, and the reported margin of error was typically about twice the standard deviation - the radius of a 95% confidence interval. Gray lines show the transports corresponding to individual profiles. The black solid line and the dash lines represent the mean value and the upper and lower 2σ of the average, respectively. As shown in Figure 5, the transports represented both directions (northward and southward), which was due to the fact that the Argo floats were located on both sides of the eddy centers. In the surface layer, eddies had weaker effects on the heat transport (Figure 5a). As the depth increased, the heat transports sharply increased until around 70 m, and then they gradually weakened with depth. Below 400 m, the eddies had very small heat transports. The obvious salt transports could only be found in the upper 200 m, and most of the transports were in the top 100-m layer (Figure 5b). These results are consistent with the results of individual eddies investigated by CTD in section 3.1.

[23] The variation of heat transports with depth was significantly different from that of salt transports with depth. To investigate this, the thermocline and halocline were examined. The thermocline in the SCS was defined as the range of depths where the rate of vertical temperature change is greater than $0.05°C\ m^{-1}$. Following the oceanic investigation standard of the Chinese State Technological Supervisory Bureau, the vertical salinity gradient $ds/dz = 0.01\ m^{-1}$ was defined as the lowest index of the SCS halocline. Using the 375 Argo profiles, we found that the vertical ranges of the thermocline and halocline were 35–165 m and 10–75 m, respectively, as shown in Figures 5a and 5b (dash-dotted lines). The heat transports mainly occurred in the thermocline, as shown in Figure 5. In the upper mixed layer, it has been seen that the warm or cold water induced by eddies can mix well with surrounding water, and, thus, the temperature anomalies can be relatively small (see Figure 9b in *Chen et al.* [2011a]). Therefore, the transports are relatively weak. Similar to the heat transports, the strong salt transports in our study mainly occurred in the halocline. Due to the existence of a barrier layer in the SCS [*Du et al.*, 2004; *Zeng et al.*, 2009], the halocline was much shallower than the thermocline. As a result, we observed larger salinity anomalies, and thus stronger salt transports, in the surface layer in spite of small temperature anomalies and weaker heat transports. In the deep layer below 200 m, the

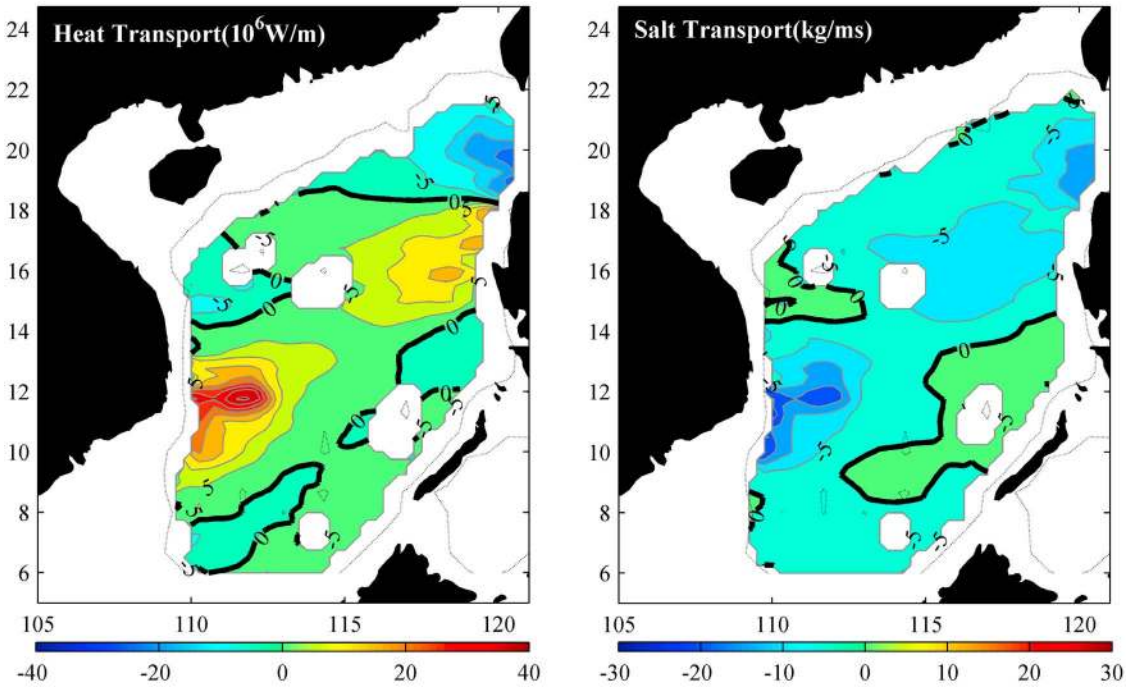

Figure 6. Meridional eddy heat and salt transport in the SCS. Contour intervals are 5 × 10^6 W/m and 5 kg/ms, respectively. The dashed line is the 400-m isobath.

heat transports decreased as the depth increased, but the salt transports changed little. This was because the vertical salinity gradient was weak in the subsurface layer. Despite the mesoscale eddy deepening or the shoaling of the isohaline, less salinity anomaly could be observed. This situation was consistent with the conclusions by *Chen et al.* [2010b] that the eddy pair off eastern Vietnam can lead to stronger temperature variability in the upper 380 m, but can only lead to stronger salinity variability in the upper 150 m.

[24] To summarize, due to spatially asymmetric distributions of temperature and salinity anomalies, the eddy-induced turbulent transports in the SCS directed either northward or southward. Because of strong mixing in the upper mixed layer and weak vertical temperature and salinity gradients in the deep layer, the heat and salt transports mainly occurred in the thermocline and halocline. The existence of a barrier layer made the halocline shallower than the thermocline so that stronger salt transports were observed in the surface layer in spite of weaker heat transports there.

4. Eddy Transport in the SCS Basin

[25] Because the eddy-induced turbulent heat transport in the subtropical North Pacific is largely confined to the upper ocean, *Qiu and Chen* [2005] assumed an effective depth to convert a depth-integrated heat transport to a surface value. Using the effective depth and the concurrent satellite SSH and SST, they derived the basin-scale eddy heat transport. However, due to the weaker surface heat transport in the SCS, we could not apply their method here. Instead, we estimated eddy heat and salt transports in the form of eddy diffusion (see section 2.2).

[26] Following *Stammer* [1998], $\bar{T}$ is defined as the mean temperature in the upper 1,000-m water column. *Qiu and Chen* [2005] concluded that, in the subtropical North Pacific, $\bar{T}$ should be averaged in the top 200 m where heat transport is confined. In view of the eddy transports in mesoscale eddies in the SCS (Figures 3–5), more relevant $\bar{T}$ and $\bar{S}$ in the SCS should be those averaged in the top 400 m and 200 m, respectively. We estimated the scaling factor α in the following way. From each Argo profile affected by eddies, we calculated the heat transport based on the method stated in section 3.1. The heat transport was estimated based on the diffusion coefficient method in section 2.2 using the altimeter data (for K_{E} and T_{alt}) and the 375 Argo profiles data (for the meridional gradient of the mean temperature). Therefore, we calculated the scaling factor α by $\alpha = \frac{\int_D^0 v(z)'T'(z)dz}{2K_E T_{alt}\partial \bar{T}_{Argo}/\partial y}$, where D was defined as 1,000 m when the effective observation depth of Argo profile was greater 1,000 m. Otherwise, D was the maximum effective observation depth. K_E was estimated in exactly the same place and at the same time as $v'T'$ was calculated. According to each profile's time, the characteristic timescales T_{alt} was obtained from sea surface height data at the profile's position in the subsequent 200 weeks. Then we derived α by averaging the α values from the available profiles. The overall mean α value from the 375 profiles was 0.0100 ± 0.0036.

[27] Based on the WOA01 data and 10 years of altimeter data from 1999 to 2009, the estimated meridional eddy transports of heat $[-\rho C_p \kappa \partial \bar{T}/\partial y]$ and salt $[-\rho/S_0 \kappa \partial \bar{S}/\partial y]$ in the SCS are shown in Figure 6. Here the climatological K_E, T_{alt}, $\bar{T}$ and $\bar{S}$ were taken as the annual mean at each grid point. Large poleward eddy heat transports were observed EOV with a maximum of 41 × 10^6 W/m and WOL with a

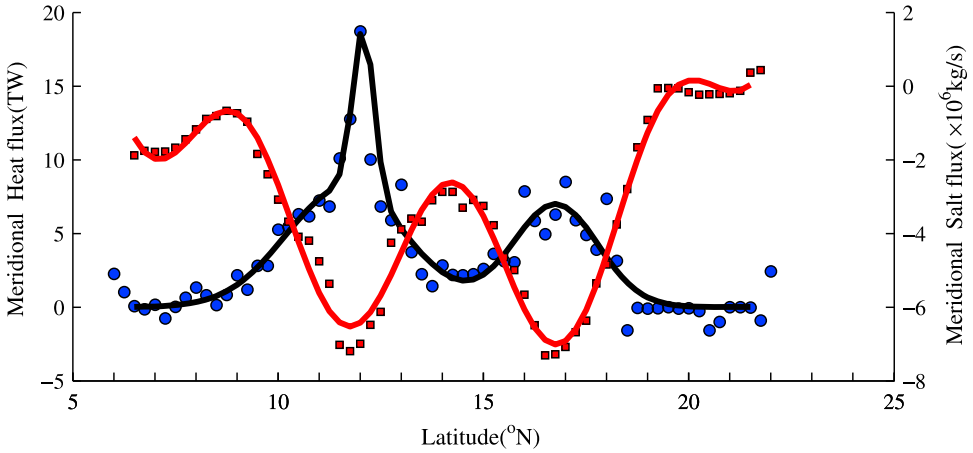

Figure 7. Zonally integrated meridional eddy heat (blue dots and the fitted black curve) and salt (red squares and the fitted red curve) transports in the SCS.

maximum of 18 × 10^6 W/m, whereas large equatorward transports were located WLS with a maximum of −22 × 10^6 W/m. These three regions corresponded to the higher eddy probability area associated with the dynamic variability of a coastal jet and the Kuroshio intrusion [*Chen et al.*, 2011a], and, therefore, tended to be continually covered by eddies. The regions of lower transports lay in the northwestern and southeastern regions in the SCS and showed good agreement with the low eddy probability area [*Chen et al.*, 2011a]. Because the temperature tended to decrease toward the poles and the sign of meridional eddy transports was solely determined by the meridional temperature gradient $-\partial\bar{T}/\partial y$, considering that the temperature gradient WLS decreased westward from the Luzon Strait (∼−1.7 × 10^{-5} °C/m to the northern SCS ∼−1.0 × 10^{-6} °C/m), the equatorward transports WLS could be attributed to the warm water intrusion of the Kuroshio that changes the sign of the meridional temperature gradient. The southwestward propagation of mesoscale eddies generated in this region [*Chen et al.*, 2011a] may also help the equatorward transport. We saw that the salt transports were mostly similar to the heat transports but in the equatorward direction in most regions due to the fact that the mean salinity in the upper 200 m in the SCS tended to decrease toward the equator (not shown). This could be attributed to the water mass in the SCS originating from the Pacific through Luzon Strait. Precipitation in the SCS is basically opposite phase to the mean salinity (not shown), suggesting that regional precipitation may also contribute to the salinity distribution. The magnitude of salt transports ranged from −19 kg/ms to 1 kg/ms.

[28] The zonally integrated meridional eddy heat and salt transports are shown in Figure 7. As expected, the largest poleward eddy heat transport of 18 TW was observed at 12°N, and the second largest was found at 17°N of 7 TW. In the latitudinal band of 19°N–22°N, a weaker equatorward transport was present, which was attributed to the narrower integration domain. In contrast to the poleward heat transport, the equatorward salt transport could be observed at nearly all latitudinal bands. The obvious salt transport was also seen at 12°N and 17°N, with a maximum of −7 × 10^6 kg/s. In general, large eddy heat and salt transports were located where currents were strong. *Gan and Qu* [2008] found that the current variability is positively correlated with current strength. In fact, the turbulent transports are associated with current variability induced by baroclinic instability in the SCS (section 5).

[29] We used eddy heat transport as an example to understand the controlling processes of the eddy transport. It was found that the eddy heat transport is proportional to T_{alt}, K_E (EKE) and the meridional gradient of the mean temperature averaged in the upper water column. Figure 8 presents the $\partial\bar{T}/\partial y$ distributions in the SCS. As expected, the pattern of the eddy heat transport was largely determined by the mean temperature gradient, as eddy transport was the result of eddy acting on the mean flow. The larger temperature gradient in WLS and WOL was attributed to the cyclonic

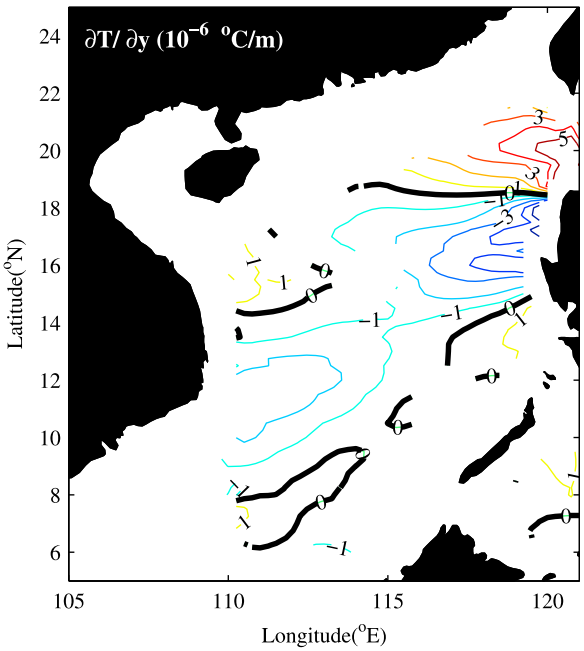

Figure 8. The meridional gradient of the mean temperature in the upper 400 m.

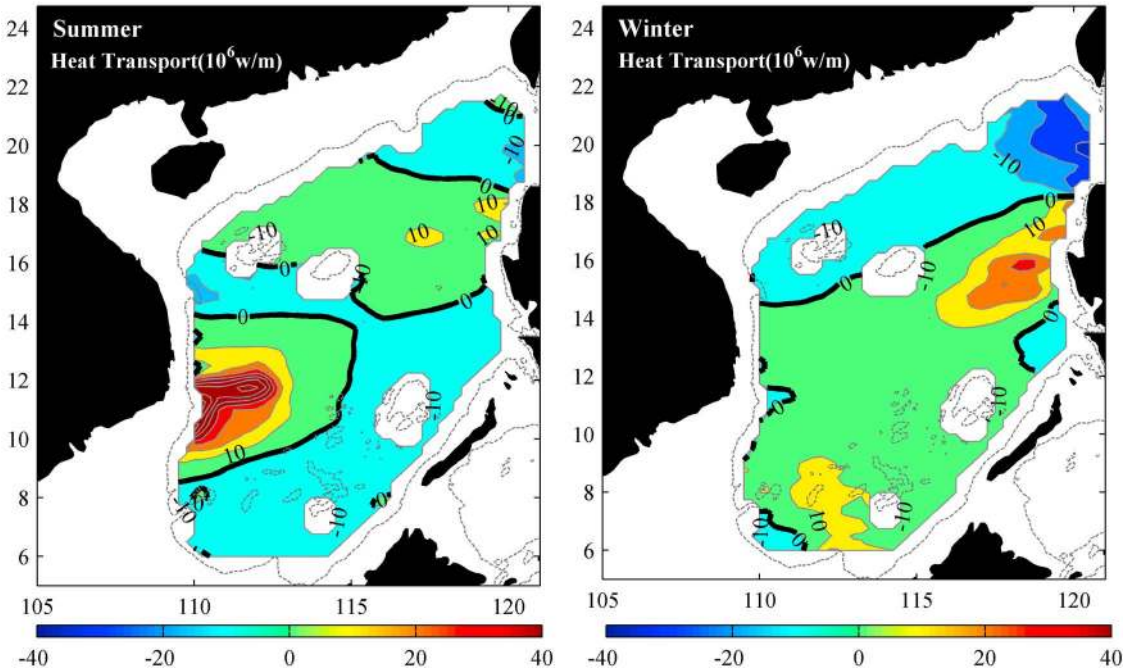

Figure 9. Meridional eddy heat transport in (left) summer and (right) winter. The contour interval is 10 × 10^6 W/m. The dashed line is the 400-m isobath.

gyre in the Northern SCS, whereas the larger gradient in EOV was due to the separation of upwelling jet from the Vietnamese coast in summer (section 5). In addition, the quasistationary Luzon Cold Eddy induced the West Luzon Front in the temperature field [*Belkin and Cornillon*, 2003]. However, the distribution of eddy transport may not totally resemble to that in temperature gradient. For example, the maximal temperature gradient in WOL was not necessary having large eddy heat transport. These discrepancies motivated us to seek other elements contributed to the eddy transport. It has been found that the spatial distribution of heat transport resembles to that of EKE [*He et al.*, 2002; *Chen et al.*, 2009]. The distribution of T_{alt}, however, showed obvious discrepancy with that of the heat transport. The larger T_{alt} was observed in the southeastern SCS, whereas the smaller T_{alt} was seen along the path of the SCS western boundary current due to stronger intraseasonal variability in these areas [*Zhuang et al.*, 2010]. The correlation between relative strong eddy transport and EKE in the EOV, WLS and WOL was thus investigated below.

5. Seasonal Modulations in Eddy Transports

[30] The SCS circulation presents a basin-wide cyclonic circulation pattern, which is merged from the northern and the southern cyclonic gyres, in winter [*Wyrtki*, 1961; *Qu*, 2000]. In the Luzon Strait, although the intrusion of the Kuroshio into the SCS can occur during any season [*Yuan et al.*, 2006; *Chen et al.*, 2011b, 2011c], winter is the most favorable season for the intrusion. In summer, the seasonal circulation pattern in the SCS consists of a weak cyclonic northern gyre and an anti–cyclonic southern gyre [*Wu et al.*, 1998; *Su*, 2005] with a strong eastward jet shooting away from the Vietnamese coast [*Fang et al.*, 2002; *Xue et al.*, 2004; *Gan et al.*, 2006]. Considering that large eddy transports are located where stronger currents are found, we investigated the effect of current seasonal variability on eddy transports in these regions.

[31] We examined the eddy heat transport in summer (June–August) and winter (December–February). Similar to the above paragraphs, we first estimated the scaling factors α. Because of the similar characteristics of eddy transports for all of the profiles (Figure 5), we ignore the spatial difference but only separate these profiles into different seasons to ensure enough sampling. The scaling factors for summer and winter were 0.008 and 0.009, respectively. A large magnitude (with a maximum of 90 × 10^6 W/m) eddy heat transport was found over a broad area EOV in summer, whereas a quite weak transport (<10 × 10^6 W/m) was observed in winter at the same location (Figure 9). In contrast to the region EOV, relatively large transports in the WLS and WOL regions were observed in winter.

[32] Figures 10 and 11 present the σ_θ structures and zonal geostrophic velocity profiles along 111°E in EOV and 119°E in WLS and WOL in August and December. Due to a great loss of heat at the sea surface and stronger mixing, the vertical density gradient in the water column in WLS was greatly weakened in winter (19°N–22°N in Figures 11a and 11c). The stratification EOV also became weak in winter, but only to a certain degree (Figures 10a and 10c; also see details in Figure 14). In contrast to those two regions, the vertical density gradient WOL strengthened in winter (14°–18°N in Figures 11a and 11c; also see details in Figure 14). Using altimeter and Argo temperature profile data, *Chen et al.* [2011a] concluded that a cyclonic eddy shoals the thermocline while considerably strengthening the intensity of the thermocline. The stronger gradient WOL in winter may be attributed to the effect of the Luzon Cold Eddy [*Shaw et al.*, 1999] as colder water moves upward in the eddy center. We saw that the zonal current EOV was strong in August, with a maximum eastward velocity of 0.3 m/s. It weakened in

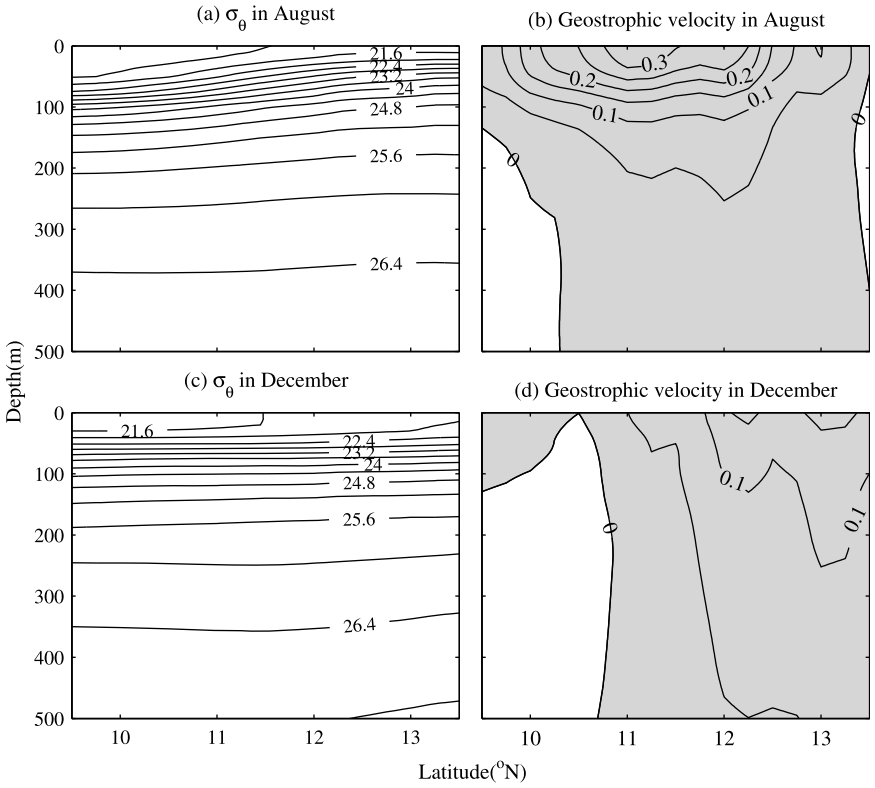

Figure 10. Density structures and zonal geostrophic velocities along 111°E. Contour intervals are 0.4 for density and 0.05 m/s for velocity.

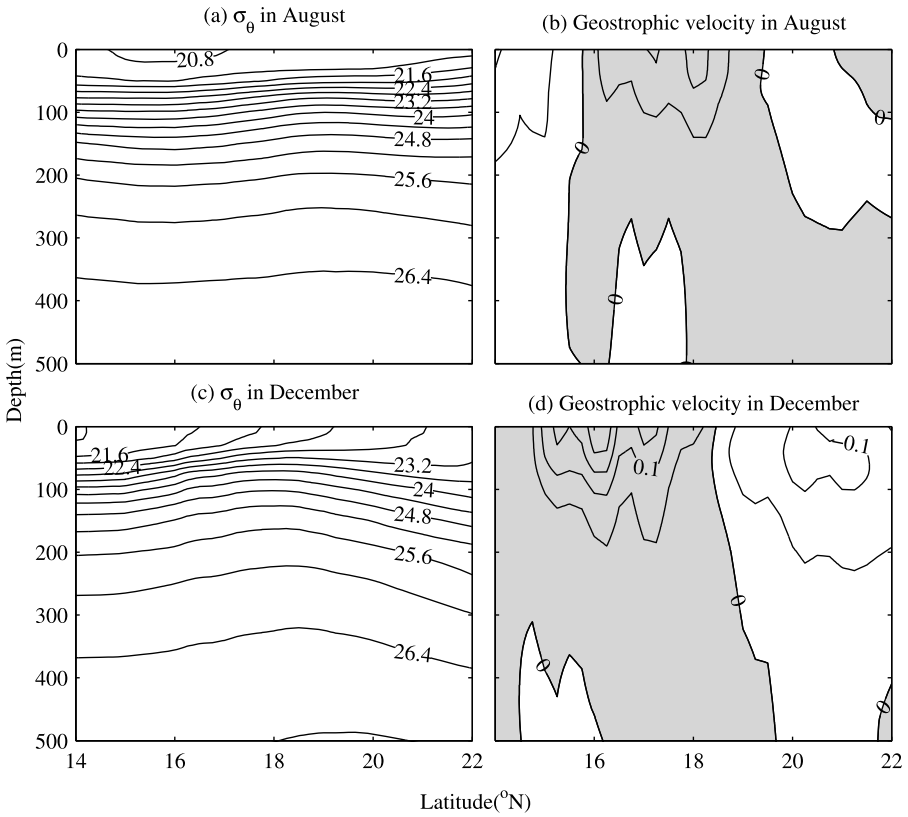

Figure 11. Same as Figure 10, except along 119°E.

Table 1. Parameter Values Appropriate for EOV in August and for WLS and WOL in December

Parameter	EOV (Aug)	WLS (Dec)	WOL (Dec)
f_o	3.024×10^{-5} s^{-1}	5.094×10^{-5} s^{-1}	4.009×10^{-5} s^{-1}
β	2.233×10^{-11} s^{-1} m^{-1}	2.138×10^{-11} s^{-1} m^{-1}	2.195×10^{-11} s^{-1} m^{-1}
U_1	0.240 ms^{-1}	−0.092 ms^{-1}	0.132 ms^{-1}
U_2	0.055 ms^{-1}	−0.065 ms^{-1}	0.041 ms^{-1}
H_1	50 m	50 m	50 m
H_2	150 m	150 m	150 m
ρ_1	21.6 σ_θ	22.8 σ_θ	21.8 σ_θ
ρ_2	24.0 σ_θ	24.1 σ_θ	24.1 σ_θ
ρ_3	26.7 σ_θ	26.8 σ_θ	26.8 σ_θ
γ_2	0.90	0.48	0.85
l	1.0×10^{-5} m^{-1}	2.0×10^{-5} m^{-1}	1.0×10^{-5} m^{-1}

December (Figures 10b and 10d). In contrast, we observed a strong zonal current WLS (WOL) in December with a maximum westward (eastward) velocity of 0.1 m/s (0.2 m/s) (Figures 11b and 11d). Compared with the situations in summer, the stratification weakened EOV and WLS but strengthened WOL, whereas the vertical velocity shear tended to be weaker EOV but stronger WLS and WOL in winter. The seasonal variability of the stratification and vertical velocity shear of the background flows synchronized with the seasonal modulations of the eddy transports in these three regions, motivating us to seek a relationship between baroclinic instability and the eddy transports.

[33] The heat transport in the SCS and the EKE present similar spatial distribution and seasonal variability [*He et al.*, 2002; *Chen et al.*, 2009]. Using a 2½-layer reduced-gravity model, *Qiu* [1999] pointed out that the seasonal modulation of the EKE field is a manifestation of baroclinic instability in intensity. Based on Figures 9–11 and following *Qiu* [1999], we hypothesize that because of the combination of the vertical velocity shear, stratification, and position of the current, the zonal flow EOV (or WLS or WOL) becomes baroclinically unstable in summer (winter), and this instability weakens or dissipates in winter (summer). Baroclinic instability facilitates the transformation of mean flow potential energy to EKE. Because the eddy transport is proportional to EKE (see section 2.2), it is reasonable that the obvious seasonal cycle of EKE in the SCS leads to the seasonal modulations of eddy transports. That is to say, baroclinic instability contributes to the seasonal change in EKE, and thus affects the seasonal variability of eddy transports.

[34] To verify this hypothesis, we followed *Qiu* [1999] and considered the vertically sheared system of these zonal currents in a 2½-layer reduced-gravity model. In Table 1, we list the parameter values appropriate for the region EOV in August and the regions WLS and WOL in December. The above paragraphs show that bulk of the eddy heat transport is confined to the upper 200-m layer. In addition, the seasonal and permanent thermoclines in the SCS are located at about 40 m and 120 m [*Chen et al.*, 2011a; *Lan et al.*, 2006], respectively. So we set H_1 and H_2 as 50 m and 150 m, respectively. The reference latitudes for f_0 and β in the three regions were defined at 12°N, 20.5°N, and 16°N, respectively. Other parameters were estimated from the monthly climatological data sets of WOA01. Using equation (5) and the values listed in Table 1, we calculated the growth rates (kc_i) of the unstable waves in the three regions as a function of the zonal wave number k (Figure 12). Although the three systems were unstable under the given conditions, the growth rates were substantially different from each other. The most unstable wave in the region EOV in August had $kc_i = 0.0372$ day^{-1}, or a time scale of 27 days, whereas the time scale in the WLS and WOL regions in December was about 60 days. The window within which the unstable waves were permissible WLS was considerably broader than that for EOV and WOL. Using similar analytical methods for the region EOV in December and WLS and WOL in August, the solutions to equation (5) indicated that the regions were dynamically stable ($kc_i \equiv 0$) in these situations. The result of the stability analysis supports the notion that the seasonal change in eddy transports or EKE reflected the seasonal modulation of the baroclinic instability.

[35] To test the sensitivity of the vertical velocity shear, we plotted the maximum growth rates for the three regions as a function of U_1 and U_2 for the parameter values listed in Table 1 (Figure 13). The stippled areas correspond to the possible value for the baroclinic instability of each region in particular month. Among the three regions, the region WLS was most likely to become baroclinically unstable. In contrast, the region EOV could not reach an unstable state except with a strong vertical shear. Why the discrepancy?

[36] The necessary conditions for the instabilities WLS, and the instabilities EOV and WOL are $|U_1 - U_2| > \delta_1\gamma_2\lambda^2\beta$ and $U_1 > (1 + \gamma_2)U_2 + \gamma_2\lambda^2\beta$, respectively (refer to the derivation process in *Qiu* [1999]). Therefore, a stronger vertical velocity shear ($U_1 - U_2$), a small stratification ratio γ, and a higher latitude would help meet the conditions, and thereby increase the potential for baroclinic instability to occur.

[37] For the values corresponding to the region WLS listed in Table 1, $\gamma_2\lambda^2\beta = 0.005$ m/s. Thus, in order to develop instability, the vertical velocity shear only needed to exceed the critical value 0.005 m/s in December. That is why there existed a large area in the ($U_1 - U_2$) space of Figure 13b where instability could happen. Although the vertical shear in the region WLS was weakest among the three systems

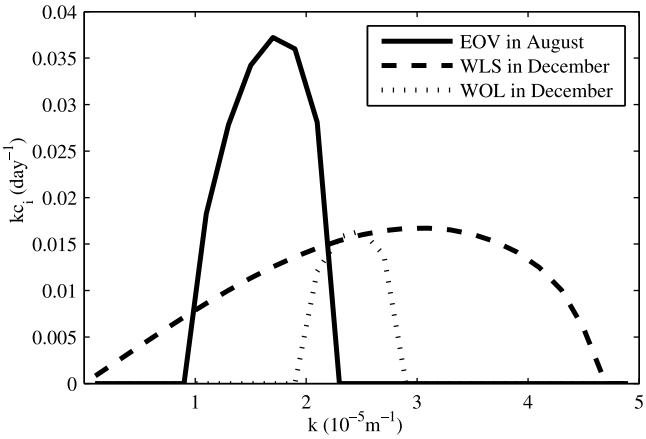

Figure 12. Growth rate as a function of zonal wave number, k, calculated from equation (5). The solid line is the result for EOV in August; dashed line and dotted lines are the results for WLS and WOL in December, respectively.

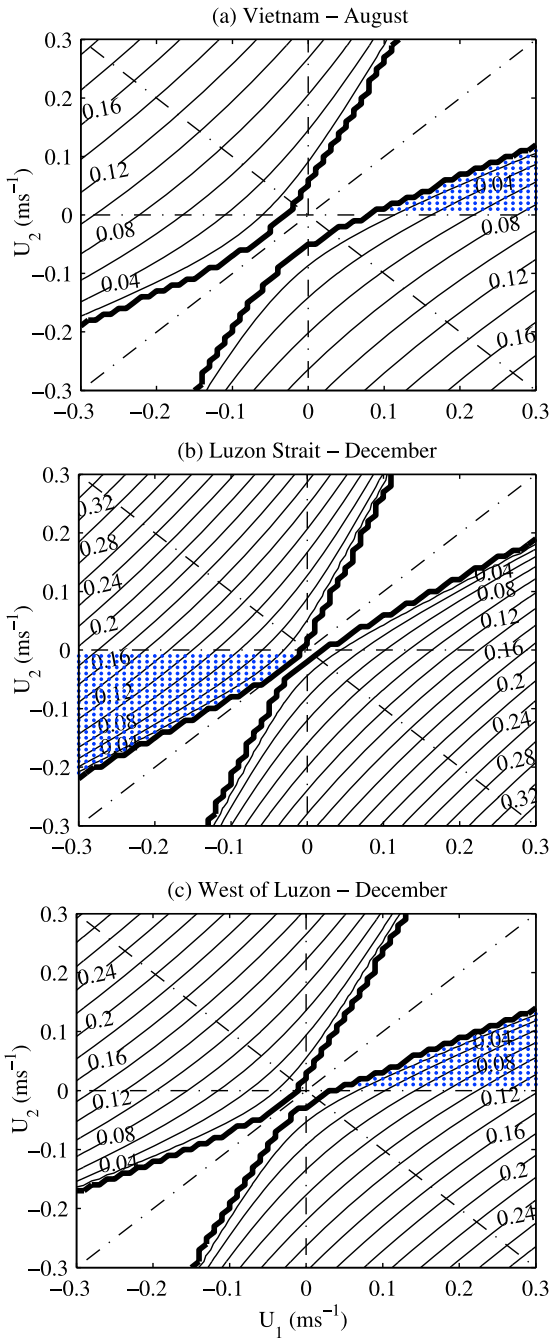

Figure 13. Maximum growth rate dependence on U_1 and U_2 EOV, WLS, and WOL for the parameter values listed in Table 1. The region between the two thick lines is dynamically stable. The stippled areas correspond to the possible value for the baroclinic instability of each region in a specific month.

(Table 1), the region WLS was the most likely area to become baroclinically unstable (Figure 13), which is attributed to the small stratification ratio in December (Figure 14) and its presence in a relatively higher latitude band.

[38] In the region EOV, the condition indicates that U_1 had to exceed $(1 + \gamma_2)U_2 + \gamma_2\lambda^2\beta = 0.188$ m/s in order for the system to become baroclinically unstable in August. Considering that the stratification ratio in that region was larger in the whole year (Figure 14) and that the region EOV is located in a lower latitude, we can draw the conclusion that the baroclinic instability in the region EOV was mainly due to the stronger vertical velocity shear in August.

[39] The critical value of U_1 for the region WOL to become baroclinically unstable was 0.123 m/s in December. In contrast to the region EOV in August, the region WOL in December had a weaker vertical velocity shear and similar stratification ratio. We also found that the region WOL was baroclinically stable in August. However, the stratification ratio in the region WOL in December was stronger than in August. Therefore, the higher latitude associated with the vertical shear was critical for the baroclinic instability in the region WOL.

6. Discussion

6.1. The Estimation of Eddy Transport

[40] Baroclinic instability arising from zonal current may lead to the formation of mesoscale eddies, and thus eddy transport in the cross-current direction (northward or southward). In EOV, the basic northeastward current may have an impact on the estimation of the northward eddy transport in summer as shown in Figure 15a. To obtain the eddy transport without the transport due to the basic currents, we derived the northward component of the cross-current transport in EOV (Figure 15b) by taking the angle between the jet and the x-axis as 29°, based on Figures 8 and 9. Although there is no obvious discrepancy between Figures 15a and 15b, the northward component of the cross-current transports is unexpectedly larger, suggesting that the contribution of the basic current to eddy heat transport is much smaller than the cross-current transports. The reason for this may be due to the relatively small deflection angle of the jet in EOV.

[41] It is noted that due to the limited number of Argo profiles, we adopted the constant scaling factor α in the entire SCS. In order to better derive the spatial characteristics of α, additional hydrological data are needed.

6.2. The Instability Analysis

[42] According to the depths of larger eddy transport and the thermocline, the thickness of top and second layers was selected as 50 m and 150 m, respectively. To better examine

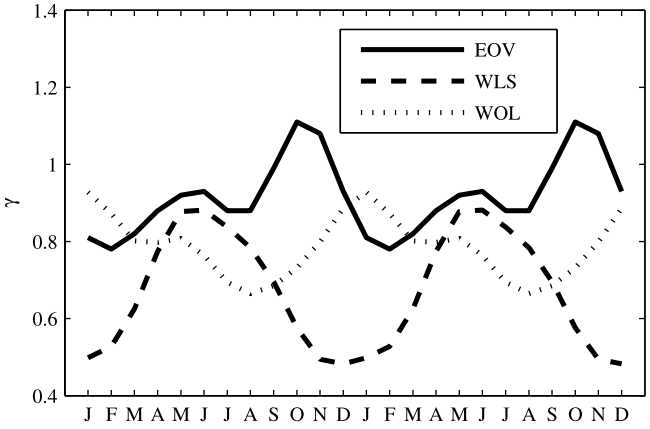

Figure 14. Seasonal cycle of the stratification ratio for EOV, WLS, and WOL.

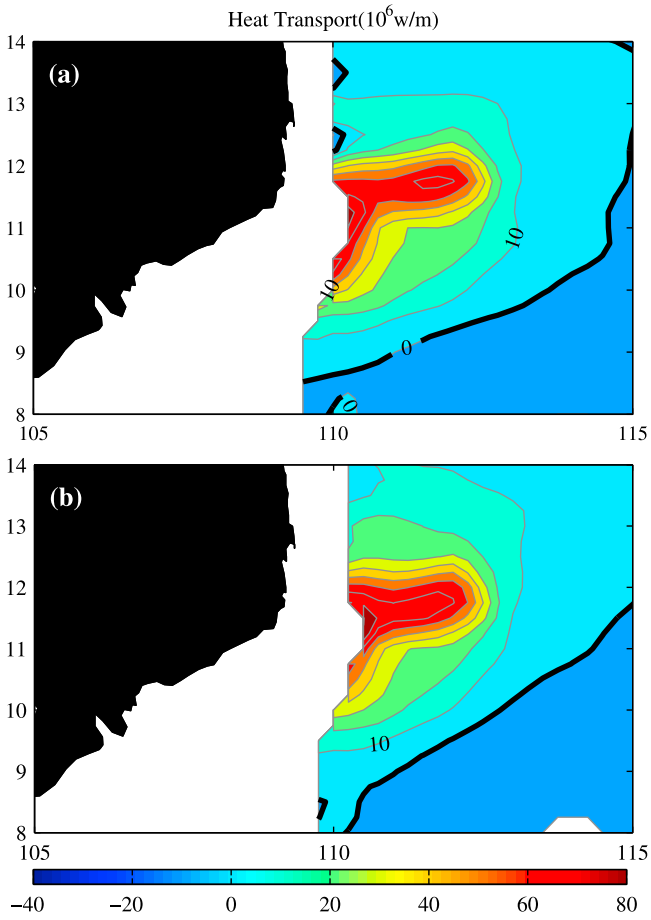

Figure 15. Meridional eddy heat transport in EOV in summer. (a) Same as Figure 9b, except only in the EOV; (b) the northward component of the cross-current transport in the EOV. The contour interval is 10×10^6 W/m.

the release of potential energy by baroclinic instability associated with the interface tilts in different depth, we assumed that the 2½-layer model has 150 m upper layer and 300 m second layer on the motionless bottom layer. Using similar analytical methods for the three regions (WOL, WLS and EOV) in different seasons, the results showed that the water column was dynamically stable except in the WLS during winter. The most unstable wave in the region WLS in December had a time scale of 52 days (Figure 16a), a slightly shorter than that of the upper layer instability (~60 days; Figure 12). However, the unstable waves were fairly longer than that for the upper layer instability. The wavelength of the most unstable wave was about 420 km, which was twice the situation of the upper layer instability. The release of potential energy in deeper layer may provide a supplement to the EKE (and thus the eddy transports) in spite of weaker eddy transports in deeper layer. To examine the eddy heat transports in the region WLS with greater depth, we used upper 800 m average $\bar{T}$. The scaling factors α, derived from the Argo profiles north of 18°N, was 0.011. The mean equatorward transports in the WLS was -11×10^6 W/m, which was 38% larger than the situation (-8×10^6 W/m) of the top 400 m (Figure 16b). Thus, the instability and eddy transport in deeper layer were non-ignorable supplements to that of the upper layer.

[43] Baroclinic instability contributes to the seasonal change in EKE, and thus affects the seasonal variability of eddy transports. Due to the fact that the 2½-layer reduced-gravity model precludes other processes, more work is needed on energy conservation between eddy and current. Herein, we followed *Qiu and Chen* [2005] and used a 1½-layer reduced-gravity model to examine whether the horizontal shear of the current (barotropic instability) contributes to the observed EKE signals. Our results showed that the meridional gradient of zonal current is not large enough for the EOV, WOL and WLS to become barotropic instability.

[44] In section 4, we examined eddy transports in basin-scale general circulation. The terminology "eddy" includes not only the circular mesoscale eddies, but also any components of the velocity field that are time-varying. Due to the fact that winter is the most favorable season for the Kuroshio into the SCS, the larger EKE in the WLS in winter may be also related to the change of current paths without the instability being invoked. Thus, evaluation of the effect of flow path on eddy transport will be very meaningful.

7. Summary

[45] Characteristics of eddy transports are fundamentally important in determining spatiotemporal variability in the

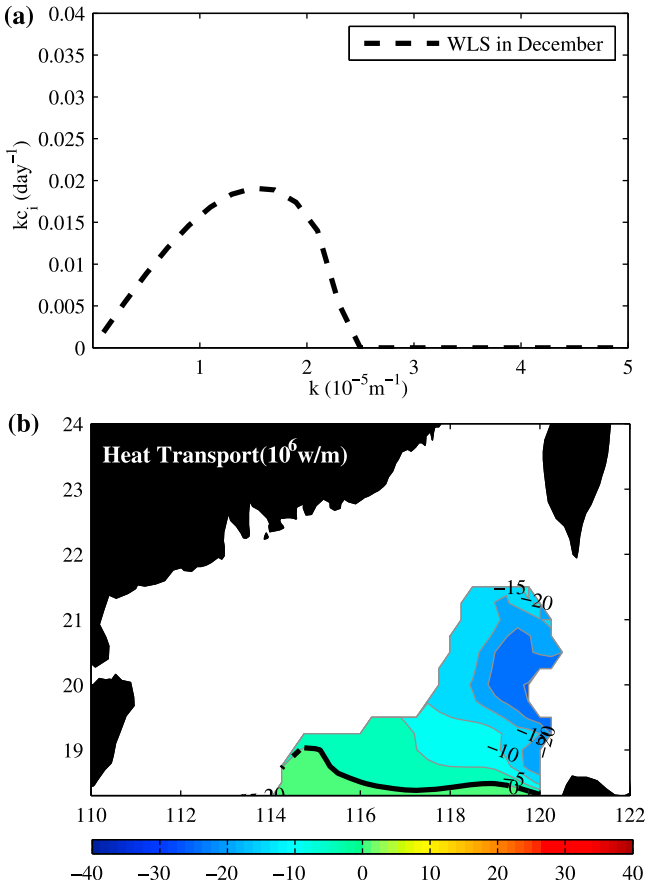

Figure 16. (a) Growth rate as a function of zonal wave number for WOL in December. (b) Annual meridional eddy heat transport in EOV. The contour interval is 5×10^6 W/m.

ocean's general circulation and its tracer distribution. So far, few studies have focused on eddy transport features in the SCS. Due to the propagation and evolution of mesoscale eddies it is, however, not easy to present the transports in mesoscale eddies. In this study, we estimated the eddy transports in the SCS basin as well as in the mesoscale eddies. The underlying physics of the observed seasonal modulations related to the eddy transports was then explored.

[46] Based on in situ data and Argo profiles, our analysis revealed that, because of strong mixing in the upper mixed layer and weak vertical temperature and salinity gradients in the deep layer, the turbulent heat and salt transports induced by mesoscale eddies mainly occurred in the thermocline and halocline. The existence of a barrier layer made the halocline shallower than the thermocline, thus stronger salt transports were observed in the surface layer despite weaker heat transports there. Asymmetric distributions of temperature and salinity anomalies to the mesoscale eddies formed net meridional turbulent heat and salt transports.

[47] Considering the confinement of eddy heat and salt transports to the thermocline and halocline, we used an eddy diffusion method to estimate the eddy transport of the basin circulation in the SCS. Large poleward eddy heat transports were observed in the region EOV in summer and in the region WOL in winter, whereas large equatorward heat transports were located in the region WLS in winter. Because the temperature tended to decrease toward the poles, the equatorward transports in the region WLS might have been due to the warm water intrusion of the Kuroshio that changes the sign of the meridional temperature gradient. The eddy salt transports were mostly similar to the heat transports but in the equatorward direction in most regions due to the fact that the mean salinity in the upper layer in the SCS tended to decrease toward the equator. This is likely because the water mass in the SCS originates from the Pacific through Luzon Strait. Regional precipitation may also contribute to the salinity distribution.

[48] Using a 2½-layer reduced-gravity model to represent the vertical velocity shear, we showed that baroclinic instability is critical to the seasonal modulations of EKE and thus the eddy transports. EOV in summer and the regions WLS and the WOL in winter were largely all baroclinically unstable, whereas the region EOV in winter and the regions WLS and WOL in summer were dynamically stable. In order to develop instability WLS, the vertical velocity shear only needed to exceed the critical value 0.005 m/s in December. WLS was the most likely area to become baroclinically unstable in winter due to small stratification and its presence in the relatively higher latitude band. With strong stratification and low latitude, a strong vertical velocity shear maintained the baroclinic instability EOV. In contrast to the region EOV in summer, the region WOL in winter had a weaker vertical velocity shear but a similar stratification ratio. We also found that the system was baroclinically stable in summer. However, the stratification ratio WOL was stronger in winter than in summer. Therefore, the relatively higher latitude associated with the vertical shear was critical for baroclinic instability WOL.

[49] **Acknowledgments.** The altimeter data were obtained from the Aviso website and the Argo data from the USGODAE website. This work is supported by National Basic Research Program of China (Grant No. 2011CB403504), National Natural Science Foundation of China (Grant Nos. 40830851 and 41106027), Hong Kong Research Grant Council under project 601009, Open Fund of the Key Laboratory of Ocean Circulation and Waves, Chinese Academy of Sciences (KLOCAW1202) and the Knowledge Innovation Program of the Chinese Academy of Sciences (SQ201105). We would like to thank two anonymous reviewers for comments that helped to improve the manuscript.

References

Belkin, I., and P. Cornillon (2003), SST fronts of the Pacific coastal and marginal seas, *Pac. Oceanogr.*, *1*(2), 90–113.

Boyer, T., S. Levitus, H. Garcia, R. Locarnini, C. Stephens, and J. Antonov (2005), Objective analyses of annual, seasonal, and monthly temperature and salinity for the world ocean on a 0.25° grid, *Int. J. Climatol.*, *25*, 931–945, doi:10.1002/joc.1173.

Chaigneau, A., A. Gizolme, and C. Grados (2008), Mesoscale eddies off Peru in altimeter records: Identification algorithms and eddy spatio-temporal patterns, *Prog. Oceanogr.*, *79*, 106–119, doi:10.1016/j.pocean.2008.10.013.

Chen, G., Y. Hou, X. Chu, P. Qi, and P. Hu (2009), The variability of eddy kinetic energy in the South China Sea deduced from satellite altimeter data, *Chin. J. Oceanol. Limnol.*, *27*(4), 943–954, doi:10.1007/s00343-009-9297-6.

Chen, G., Y. Hou, X. Chu, and P. Qi (2010a), Vertical structure and evolution of the Luzon Warm Eddy, *Chin. J. Oceanol. Limnol.*, *28*(5), 955–961, doi:10.1007/s00343-010-9040-3.

Chen, G., Y. Hou, Q. Zhang, and X. Chu (2010b), The eddy pair off eastern Vietnam: Interannual variability and impact on thermohaline structure, *Cont. Shelf Res.*, *30*(7), 715–723, doi:10.1016/j.csr.2009.11.013.

Chen, G., Y. Hou, and X. Chu (2011a), Mesoscale eddies in the South China Sea: Mean properties, spatiotemporal variability, and impact on thermohaline structure, *J. Geophys. Res.*, *116*, C06018, doi:10.1029/2010JC006716.

Chen, G., P. Hu, Y. Hou, and X. Chu (2011b), Intrusion of the Kuroshio into the South China Sea, in September 2008, *J. Oceanogr.*, *67*(4), 439–448, doi:10.1007/s10872-011-0047-y.

Chen, G., Y. Hou, and X. Chu (2011c), Water exchange and circulation structure near the Luzon Strait in early summer, *Chin. J. Oceanol. Limnol.*, *29*, 470–481, doi:10.1007/s00343-011-0198-0.

Dippner, J., K. Nguyen, H. Hein, T. Ohde, and N. Loick (2007), Monsoon-induced upwelling off the Vietnamese coast, *Ocean Dyn.*, *57*(1), 46–62, doi:10.1007/s10236-006-0091-0.

Du, Y., D. X. Wang, P. Shi, P. F. Guo, and J. Chen (2004), Seasonal variation of the barrier layer in the South China Sea and its relationship to the sea surface flux (in Chinese), *Chin. J. Atmos. Sci.*, *28*(1), 101–111.

Fang, W., G. Fang, P. Shi, Q. Huang, and Q. Xie (2002), Seasonal structures of upper layer circulation in the southern South China Sea from in situ observations, *J. Geophys. Res.*, *107*(C11), 3202, doi:10.1029/2002JC001343.

Gan, J., and T. Qu (2008), Coastal jet separation and associated flow variability in the southwest South China Sea, *Deep Sea Res., Part I*, *55*(1), 1–19, doi:10.1016/j.dsr.2007.09.008.

Gan, J., H. Li, E. Curchitser, and D. Haidvogel (2006), Modeling South China Sea circulation: Response to seasonal forcing regimes, *J. Geophys. Res.*, *111*, C06034, doi:10.1029/2005JC003298.

He, Z., D. Wang, and J. Hu (2002), Features of eddy kinetic energy and variations of upper circulation in the South China Sea, *Acta Oceanol. Sin.*, *21*(2), 305–314.

Hu, J., H. Kawamura, H. Hong, and Y. Qi (2000), A review on the currents in the South China Sea: Seasonal circulation, South China Sea warm current and Kuroshio intrusion, *J. Oceanogr.*, *56*(6), 607–624, doi:10.1023/A:1011117531252.

Hu, J., J. Gan, Z. Sun, J. Zhu, and M. Dai (2011), Observed three-dimensional structure of a cold eddy in the southwestern South China Sea, *J. Geophys. Res.*, *116*, C05016, doi:10.1029/2010JC006810.

Itoh, S., and I. Yasuda (2010), Water Mass Structure of Warm and Cold Anticyclonic Eddies in the Western Boundary Region of the Subarctic North Pacific, *J. Phys. Oceanogr.*, *40*, 2624–2642, doi:10.1175/2010JPO4475.1.

Kamenkovich, I., W. Cheng, C. Schmid, and D. E. Harrison (2011), Effects of eddies on an ocean observing system with profiling floats: Idealized simulations of the Argo array, *J. Geophys. Res.*, *116*, C06003, doi:10.1029/2010JC006910.

Lan, J., Y. Bao, F. Yu, and S. Sun (2006), Seasonal variabilities of the circulation and thermocline depth in the South China Sea deep water basin, *Adv. Mark. Sci.*, *24*(4), 436–445.

Nan, F., Z. He, H. Zhou, and D. Wang (2011), Three long-lived anticyclonic eddies in the northern South China Sea, *J. Geophys. Res.*, *116*, C05002, doi:10.1029/2010JC006790.

Qiu, B. (1999), Seasonal eddy field modulation of the North Pacific Subtropical Countercurrent: TOPEX/Poseidon observations and theory, *J. Phys.*

Oceanogr., *29*(10), 2471–2486, doi:10.1175/1520-0485(1999)029<2471:SEFMOT>2.0.CO;2.

Qiu, B., and S. Chen (2005), Eddy-induced heat transport in the subtropical North Pacific from Argo, TMI and altimetry measurements, *J. Phys. Oceanogr.*, *68*, 499–501.

Qu, T. (2000), Upper-layer circulation in the South China Sea, *J. Phys. Oceanogr.*, *30*(6), 1450–1460, doi:10.1175/1520-0485(2000)030<1450:ULCITS>2.0.CO;2.

Roemmich, D., J. Gilson, B. Cornuelle, and R. Weller (2001), Mean and time-varying meridional transport of heat at the tropical/subtropical boundary of the North Pacific Ocean, *J. Geophys. Res.*, *106*, 8957–8970, doi:10.1029/1999JC000150.

Shaw, P. T., S. Y. Chao, and L. L. Fu (1999), Sea surface height variations in the South China Sea from satellite altimetry, *Oceanol. Acta*, *22*(1), 1–17, doi:10.1016/S0399-1784(99)80028-0.

Stammer, D. (1997), Global characteristics of ocean variability estimated from regional TOPEX/POSEIDON altimeter measurements, *J. Phys. Oceanogr.*, *27*(8), 1743–1769, doi:10.1175/1520-0485(1997)027<1743:GCOOVE>2.0.CO;2.

Stammer, D. (1998), On eddy characteristics, eddy transports, and mean flow properties, *J. Phys. Oceanogr.*, *28*(4), 727–739, doi:10.1175/1520-0485(1998)028<0727:OECETA>2.0.CO;2.

Su, J. (2005), Overview of the South China Sea circulation and its dynamics, *Acta Oceanol. Sin.*, *27*(6), 1–8.

Wang, D., H. Xu, J. Lin, and J. Hu (2008), Anticyclonic eddies in the northeastern South China Sea during winter 2003/2004, *J. Oceanogr.*, *64*(6), 925–935, doi:10.1007/s10872-008-0076-3.

Wu, C., P. Shaw, and S. Chao (1998), Seasonal and interannual variations in the velocity field of the South China Sea, *J. Oceanogr.*, *54*(4), 361–372, doi:10.1007/BF02742620.

Wunsch, C. (1999), Where do ocean eddy heat fluxes matter? *J. Geophys. Res.*, *104*(C6), 13,235–13,249, doi:10.1029/1999JC900062.

Wyrtki, K. (1961), Physical oceanography of the southeast Asian waters, *NAGA Rep. 2*, Univ. of Calif., San Diego, La Jolla.

Xue, H., F. Chai, N. Pettigrew, D. Xu, M. Shi, and J. Xu (2004), Kuroshio intrusion and the circulation in the South China Sea, *J. Geophys. Res.*, *109*, C02017, doi:10.1029/2002JC001724.

Yuan, D., W. Han, and D. Hu (2006), Surface Kuroshio path in the Luzon Strait area derived from satellite remote sensing data, *J. Geophys. Res.*, *111*, C11007, doi:10.1029/2005JC003412.

Zeng, L., Y. Du, S. P. Xie, and D. Wang (2009), Barrier layer in the South China Sea during summer 2000, *Dyn. Atmos. Oceans*, *47*(1–3), 38–54, doi:10.1016/j.dynatmoce.2008.08.001.

Zhuang, W., S. P. Xie, D. X. Wang, B. Taguchi, H. Aiki, and H. Sasaki (2010), Intraseasonal variability in sea surface height over the South China Sea, *J. Geophys. Res.*, *115*, C04010, doi:10.1029/2009JC005647.